Inorganic Chemistry

Article

Report of the Double-Molybdate Phase Cs₂Ba(MoO₄)₂ with a Palmierite Structure and Its Thermodynamic Characterization

Anna L. Smith,* Nathan de Zoete, Maikel Rutten, Lambert van Eijck, Jean-Christophe Griveau, and Eric Colineau

Read Online

ACCESS | Metrics & More | Article Recommendations | Supporting Information

ABSTRACT: The existence of a novel double-molybdate phase with a palmierite-type structure, $Cs_2Ba(MoO_4)_2$, is revealed in this work, and its structural properties at room temperature have been characterized in detail using X-ray and neutron diffraction measurements. In addition, its thermal stability and thermal expansion are investigated in the temperature range 298−673 K using high-temperature X-ray diffraction, leading to the volumetric thermal expansion coefficient $\alpha_V \approx 43.0 \times 10^{-6}$ K^{-1}. The compound's standard enthalpy of formation at 298.15 K has been obtained using solution calorimetry, which yielded $\Delta_f H_m°(Cs_2Ba(MoO_4)_2$, cr, 298.15 K) = −3066.6 ± 3.1 kJ·mol^{-1}, and its standard entropy at 298.15 K has been derived from low-temperature (2.1−294.3 K) thermal-relaxation calorimetry as $S_m°(Cs_2Ba(MoO_4)_2$, cr, 298.15 K) = 381.2 ± 11.8 J K^{-1} mol^{-1}.
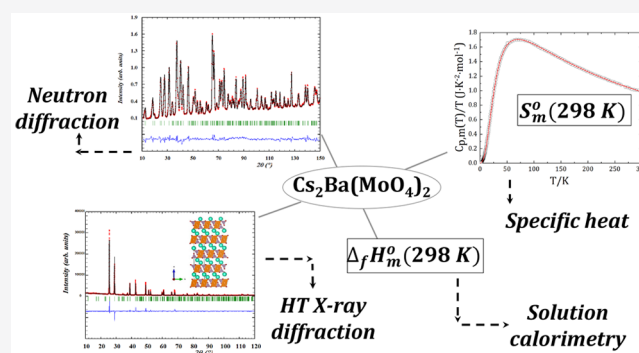
1. INTRODUCTION

A significant interest exists for molybdate materials because of their appealing optical and electronic properties for the fields of photoluminescence,[1,2] ionic conductivity,[3,4] ferroelastic and ferroelectric behavior,[5,6] and laser materials activated by lanthanide ions.[7,8] A novel double molybdate with the palmierite structure that is isostructural with $K_2Pb(SO_4)_2$,[9] i.e. trigonal in space group $R\bar{3}m$, is reported in this work. $Cs_2Ba(MoO_4)_2$ was found to form by the reaction between barium molybdate ($BaMoO_4$) and cesium molybdate (Cs_2MoO_4) at high temperatures. Our prime interest at the moment of the study was the investigation of the solubility of cesium in barium molybdate, a fission product phase expected to form at high burnup in the current generation of light water reactors (LWRs) and next-generation fast neutron reactors fueled with a ceramic $(U,Pu)O_2$ type of fuel.

Among the numerous fission products formed during irradiation of uranium dioxide and mixed uranium−plutonium oxide fuel, cesium, barium, and molybdenum are of primary importance. Cesium is classified as volatile together with iodine and tellurium and constitutes a concern for the public, as the radioactive isotopes ^{135}Cs and ^{137}Cs represent a radiological health hazard in a severe accident (SA) scenario with release to the environment. Barium belongs to the so-called semivolatile fission products, meaning that its release kinetics from the fuel matrix depend on the redox conditions of the surrounding environment.[10] Their exact speciation in irradiated fuel is rather intricate, although it is of paramount importance for SA

analysis, where the temperature and oxygen potential can vary widely.

Cesium is generated with a high yield and is present in irradiated fuel in various forms. It is mostly present as gaseous Cs and in association with other fission products in the form of Cs_2ZrO_3, Cs_2Te, and CsI at low oxygen potentials[11−13] (below about −400 kJ mol^{-1} at 1273 K according to a study by Imoto[11]). The CsI fraction remains constant irrespective of the oxygen potential, while at higher oxygen potentials (above −370 kJ mol^{-1}) cesium orthomolybdate (Cs_2MoO_4) becomes the dominant phase, the other phases becoming unstable.[11−13] The formation of Cs_2MoO_4 in fast neutron reactors in the so-called "joint oxide gaine" (JOG) layer (∼150−300 μm thickness) between the cladding and fuel above ∼7−8% FIMA (fission per initial metal atom) has been documented quite extensively.[14−20] Cs_2MoO_4 is the major constituting phase of the JOG, but other chemical elements are also found in its heterogeneous structure, notably Te, I, Zr, and Ba and the cladding components Fe and Cr.[20] The exact chemical composition of the JOG and mechanisms of its formation are still largely unknown, however, despite the clear importance for

the assessment of the fuel behavior in fast neutron reactors. Cs_2MoO_4 is known to have a lower thermal conductivity in comparison to the fuel (about 1 order of magnitude lower)[21,22] and a high thermal expansion,[23] which is detrimental to the fuel properties.

Barium, because of its large ionic radius, shows a very limited solubility in the $(U,Pu)O_2$ fuel matrix[24] and, rather, tends to form oxide precipitates. Barrachin et al.[25] recently observed in fuel test sections of the PHEBUS FPT2 test the association of barium and molybdenum at grain boundaries in the form of oxide precipitates. The thermochemical calculations by Imoto,[11] Cordfunke and Konings,[13] and Kurosaki et al.,[26] post-irradiation examinations (PIE) by Kleykamp,[24] and experimental studies by Paschoal et al.[27] and Muromura et al.[28] show that, at low oxygen potentials, the so-called gray phase, a perovskite compound of composition $(Ba_{1-x-y}Sr_xCs_y)$-$(Zr,Mo,RE,U,Pu)O_3$ (RE = rare earth only present at high burnup) is formed with a limited solubility of $BaMoO_3$,[27] while the scheelite-type $Ba(Mo_{1-x}U_x)O_4$ is the dominant phase at high oxygen potentials.[11,13,26,28] The formation of the latter phase should be even more noticeable in fast neutron reactors, which reach higher burnup levels. According to the calculations of Kurosaki et al.[26] for $(U_{0.8}Pu_{0.2}O_2)$ fuel at 100 GWd/t burnup under fast reactor circumstances, the formation of $Ba(Zr,Mo,U)O_3$ (38.6% Zr, 2.5% Mo, 58.9% U) should occur at 1273 K for an oxygen potential of around −500 to −400 kJ mol^{-1} and $Ba(Mo,U)O_4$ (94.9% Mo, 5.1% U) at a high oxygen potential (−300 to −200 kJ mol^{-1}).

Finally, molybdenum is present in metallic form, along with ruthenium, rhodium, palladium, and technetium,[24] forming the so-called "white inclusions" at low oxygen potential, and forms higher valence state componds (MoO_2, gray phase, MoO_3, scheelite, Cs_2MoO_4, etc.) with an increase in oxygen potential.[27,28] The Mo/MoO_2 redox couple plays a key role in SA analysis, as it acts as an oxygen potential buffer, which determines the chemical state of other fission products such as cesium, barium, and strontium and therefore their release behavior.[10,11,24]

Because the chemistry of cesium in irradiated fuel is of paramount importance to assess the driving force for its release into the environment, studies of its chemical speciation are a necessity. The solubility of cesium in the gray phase is reported to be low, but much less is known about its solubility in the scheelite structure $Ba(U,Mo)O_4$ formed at high oxygen potentials. With the aim of improving the evaluation of the source term in severe accident codes, a study of the solubility of cesium in barium molybdate ($BaMoO_4$) was thus carried out in our research group in the framework of the TCOFF project (thermodynamic characterization of fuel debris and fission products based on a scenario analysis of severe accident progression at the Fukushima−Daiichi nuclear power station).[29] The identification of the novel double molybdate $Cs_2Ba(MoO_4)_2$ is reported in this work, and a detailed characterization of the structure using X-ray and neutron diffraction is given. The thermal stability and thermal expansion of $Cs_2Ba(MoO_4)_2$ up to 673 K are estimated using high-temperature X-ray diffraction. Finally, the standard enthalpy of formation and standard entropy at 298.15 K are determined using solution calorimetry and thermal relaxation calorimetry, respectively.

2. EXPERIMENTAL METHODS

2.1. Sample Preparation. Barium molybdate ($BaMoO_4$) was synthesized by a solid-state reaction between barium carbonate ($BaCO_3$; >99%, Fluka) and molybenum oxide (MoO_3; 99.95%, Sigma-Aldrich), with heating in air at 1023 K twice for 12 h with an intermediate regrinding step. Cesium orthomolybdate (Cs_2MoO_4) was synthesized by a reaction between stoichiometric amounts of cesium carbonate (Cs_2CO_3; 99.99%, Alfa Aesar) and molybdenum oxide (MoO_3; 99.95%, Sigma-Aldrich) as described in ref 23. $Cs_2Ba(MoO_4)_2$ was subsequently obtained by a reaction between barium molybdate and cesium molybdate mixed in a stoichiometric ratio with heating in an alumina boat under an oxygen flow for 62 h at 1023 K with intermediate regrinding steps. Handling of the samples was done in an argon-filled glovebox, with a dry atmosphere (H_2O and O_2 contents <5 ppm), because of the known hygroscopic nature of the Cs_2MoO_4 precursor. Mixing of the precursors was done using a Retsch MM400 ball mill, with milling times ranging between 30 and 100 min.

The purity of the sample was examined by X-ray diffraction (XRD) and neutron diffraction (ND) at room temperature. The collected patterns did not reveal any secondary phases, and the sample's purity is thus expected to be better than 99%.

2.2. Powder X-ray Diffraction (XRD). A PANalytical X'Pert PRO X-ray diffractometer mounted in the Bragg−Brentano configuration with a Cu anode (0.4 mm × 12 mm line focus, 45 kV, 40 mA) and a real-time multistrip (RTMS) detector (X'Celerator) was used for the collection of X-ray diffraction patterns at room temperature. The samples were measured inside a sealed sample holder, with a Kapton foil cover, maintaining the dry argon atmosphere of the glovebox. A typical diffractogram was obtained in about 8 h, by step scanning in the angle range $10° \leq 2\theta \leq 120°$ with a step size of 0.008° (2θ). The Rietveld method as implemented in the FullProf suite[30] was used for the structural analysis.

2.3. High-Temperature X-ray Diffraction (HT XRD). High-temperature X-ray diffraction measurements were performed from room temperature up to 673 K (the maximum temperature that can be reached with our equipment) using the same diffractometer as above equipped with an Anton Paar TTK450 chamber to assess the thermal expansion and polymorphism of $Cs_2Ba(MoO_4)_2$. The data were collected under vacuum (0.02 mbar). The temperature was monitored with a Pt100 resistor. A typical isotherm measurement was performed in 6 h after 30 min of stabilization time at the measurement temperature.

2.4. Neutron Diffraction (ND). Neutron diffraction data were recorded at room temperature at the PEARL beamline at the Hoger Onderwijs Reactor at TU Delft.[31] The sample of $Cs_2Ba(MoO_4)_2$ (2.4 g) was encapsulated in a vanadium cylindrical container (50 mm high, 6 mm inner diameter) closed with a Viton O-ring in the dry argon atmosphere of the glovebox. The data were collected at a fixed wavelength (λ = 1.667 Å) for 20 h over the range $10° \leq 2\theta \leq 160°$. The Rietveld method as implemented in the FullProf suite[30] was used for the structural analysis.

2.5. Solution Calorimetry. The dissolution enthalpies of $Cs_2Ba(MoO_4)_2$, $BaMoO_4$, and Cs_2MoO_4 materials were measured using a TA Instruments Precision Solution Calorimeter (semi-adiabatic or isoperibolic calorimeter) and TAM IV thermostat. The calorimetric unit consists of a 25 mL Pyrex glass reaction vessel and stirrer system (motor and gold stirrer holding a glass ampule). The temperature changes during the experiment were monitored with a thermistor, while a heater was used for calibration during the measurement and equilibration of the initial baseline in the optimal operating range of the calorimeter before starting the experiment. The samples were encapsulated inside a 1 mL glass ampule sealed using beeswax. The latter operation was performed in the dry atmosphere of an argon-filled glovebox because of the hygroscopic nature of Cs_2MoO_4. The solid samples were dissolved in a 2 M nitric acid HNO_3 solution (molality m = 1.57 mol kg^{-1}) by breaking the bottom of the glass ampule on the sapphire breaking tip mounted at the bottom of the reaction vessel. The heat of breaking is exothermic,
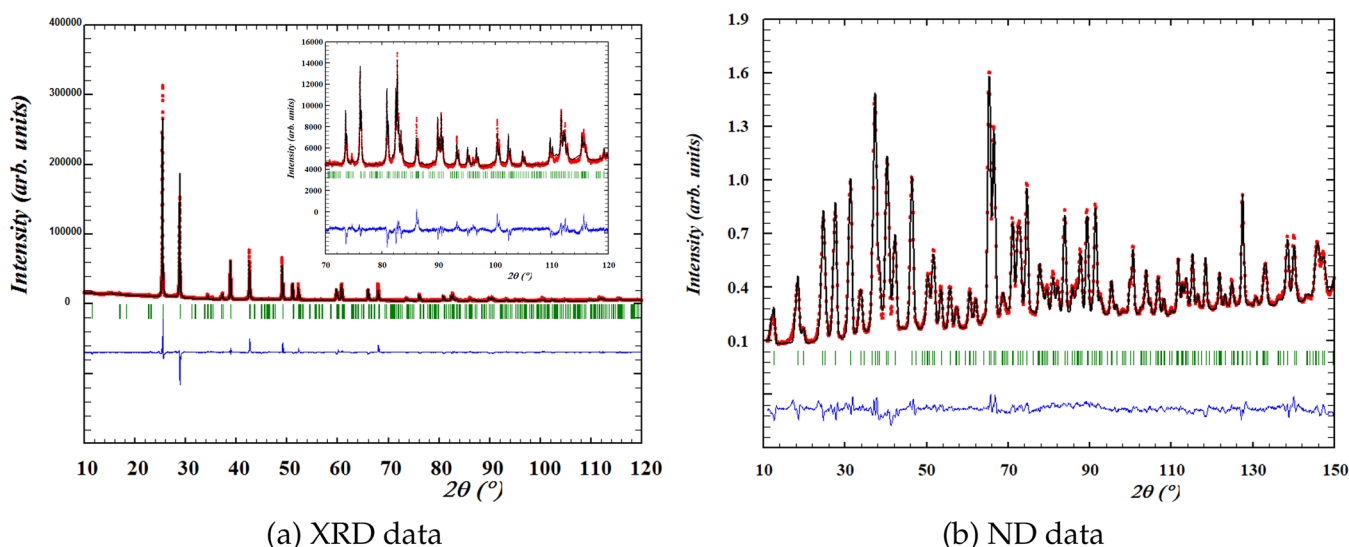
(a) XRD data   (b) ND data

Figure 1. Experimental (Y_{obs}, in red) and calculated (Y_{calc}, in black) XRD and ND patterns of $Cs_2Ba(MoO_4)_2$. The difference between calculated and experimental intensities $Y_{obs} - Y_{calc}$ is shown in blue. The angular positions of Bragg reflections are shown in green. Measurement at (a) $\lambda_{Cu\,K\alpha}$ and (b) $\lambda = 1.667$ Å.

with a value below 10 mJ, and can thus be neglected. The temperature during the measurements was maintained in the oil bath with an accuracy of $\pm 1 \times 10^{-4}$ K. Electrical calibrations were performed immediately before and after each enthalpy of reaction measurement so as to determine the energy equivalent of the system.

The enthalpy of dissolution of potassium chloride (KCl; Sigma-Aldrich, 99.7%) into $1000H_2O$ (distilled water) (molality $m = 0.05551$ mol kg^{-1}) was first measured to check the instrument accuracy, which yielded $\Delta_{diss}H_m°(1000H_2O, 298.15$ K$) = 17.510 \pm 0.024$ kJ mol^{-1}. This corresponds to a dissolution enthalpy in 500 H_2O equal to $\Delta_{diss}H_m°(500H_2O, 298.15$ K$) = 17.560 \pm 0.024$ kJ mol^{-1} after correction, as recommended by the National Bureau of Standards (NBS)[32,77] to $m = 0.111$ mol kg^{-1}, which is in very good agreement with the value recommended by the NBS:[32,34] i.e., $\Delta_{diss}H_m°(500H_2O, 298.15$ K$) = 17.584 \pm 0.017$ kJ mol^{-1}. The measured value corresponds to an enthalpy at infinite dilution of $\Delta_{diss}H_m°(\infty H_2O, 298.15$ K$) = 17.217 \pm 0.024$ kJ mol^{-1}, in very good agreement with the NBS data in refs 32 and 34, i.e. $\Delta_{diss}H_m°(\infty H_2O, 298.15$ K$) = 17.241 \pm 0.018$ kJ mol^{-1}, and that in ref 35, i.e. $\Delta_{diss}H_m°(\infty H_2O, 298.15$ K$) = 17.22$ kJ mol^{-1}. In addition, the enthalpies of formation of Cs_2MoO_4 and Na_2MoO_4 were determined with this instrument in cesium hydroxide (CsOH) and sodium hydroxide (NaOH) solutions as described in a previous work[36] and were found to be in excellent agreement with the literature data,[37−41] which gives us confidence in the reliability of the measurements. The uncertainties on the dissolution enthalpies are reported hereafter as expanded uncertainties U with a coverage factor of $k = 2$ (twice the standard deviation of the mean), which corresponds to a confidence interval of ~95%.[42]

2.6. Low-Temperature Heat Capacity. Low-temperature heat capacity measurements were performed using a thermal-relaxation method[43] on $m = 13.76 \pm 0.05$ mg in the temperature range $T = 2.1−294.3$ K mg with a PPMS (Physical Property Measurement System, Quantum Design) instrument with no applied magnetic field ($B = 0$ T). The sample was encapsulated in Stycast 2850 FT (1.96 mg) for the measurement, so as to prevent reaction with moisture in the atmosphere and to improve the heat transfer between the sample platform and this insulating oxide material. The contribution of the Stycast to the total heat capacity was subtracted from the recorded data. The contributions of the sample platform, wires, and grease were obtained by a separate measurement of an addenda curve. A second measurement was performed on a pellet of weight $m = 9.63 \pm 0.05$ mg and encapsulated in 3.52 mg of Stycast, which gave very similar results, as shown in Figure S1 in the Supporting Information. The

data obtained for the first pellet were selected for the analysis, since a higher weight and lower Stycast contribution should give a more accurate result. On the basis of previous work with this instrument with standard materials, metallic and oxide compounds, and on consideration of the error associated with the encapsulation procedure in Stycast,[44] the uncertainty was estimated to be around 1−2% in the middle range of acquisition (from 10 to 70 K) and around 3−4% near room temperature and toward the lowest temperatures.[43,44]

3. RESULTS AND DISCUSSION

3.1. Structural Characterization of the Double Molybdate $Cs_2Ba(MoO_4)_2$. During an investigation of the possible solubility of cesium in barium molybdate by mixing $BaMoO_4$ and Cs_2MoO_4 in various stoichiometric ratios ($BaMoO_4:Cs_2MoO_4 = 1 − x:x$) and heating at 1023 K under an oxygen flow for 24 h, a novel phase, not reported to this date in the literature, was identified in the collected X-ray diffraction patterns. The quaternary compound $Cs_2Ba(MoO_4)_2$ was found to form as a single phase when $BaMoO_4$ and Cs_2MoO_4 were mixed in a 1:1 ratio and mixed together with barium molybdate for $x < 0.5$ and with cesium molybdate for $x > 0.5$. The results of this study and our conclusions on the solubility of cesium in $BaMoO_4$ are described in detail in ref 45. A slight decrease in the lattice parameter of the scheelite phase was observed with increasing Cs content, which could suggest the formation of a $Ba_{1−z}Cs_zMoO_{4−z/2}$ solid solution with a limited cesium solubility. Further investigations using techniques sensitive to the oxygen environment (neutron diffraction, extended X-ray absorption fine structure spectroscopy) and molybdenum valence state (X-ray absorption near edge structure spectroscopy) would be required to ascertain this hypothesis. In any case, the major finding of this work is the acknowledgment of the possible formation of the double molybdate $Cs_2Ba(MoO_4)_2$ under reactor conditions and the consequences this could have on the irradiated fuel behavior.

The obtained quaternary phase was found to be isotypic with the palmierite mineral $K_2Pb(SO_4)_2$,[9] i.e. trigonal in space group $R\bar{3}m$, and isostructural with $K_2Ba(MoO_4)_2$[46] and $Rb_2Ba(MoO_4)_2$.[47,48] The X-ray and neutron diffraction patterns are shown in parts a and b of Figures 1, respectively.

The refined cell parameters obtained from the XRD and ND data are given in Table 1. The atomic positions and bond

Table 1. Refined Profile Parameters of $Cs_2Ba(MoO_4)_2$ from the XRD and ND Data

	XRD	ND
chemical formula	$Cs_2Ba(MoO_4)_2$	
formula wt (g mol^{-1})	723.04	
cryst syst	trigonal	
space group	$R\bar{3}m$	
Z	3	
wavelength λ (Å)	1.541/1.544	1.667
$a = b$ (Å)	6.18381(3)[a]	6.1757(2)[a]
c (Å)	23.0759(2)[a]	23.0452(9)[a]
cell volume V (Å^3)	764.191(8)	761.18(4)
d-space range (Å)	0.89–8.83	0.78–8.35

[a]The standard uncertainties obtained from the refinement are underestimated by about 1 order of magnitude.

lengths obtained from the Rietveld refinement of the ND data are given in Tables 2 and 3, respectively. The calculated and measured diffraction intensities showed good agreement for both the XRD and ND data, which gives us confidence in the structural model adopted.

$Cs_2Ba(MoO_4)_2$ is made of layers in the *ab* plane of corner-sharing BaO_6 octahedra and MoO_4 tetrahedra alternating with bilayers of CsO_{10} decahedra sharing faces with the BaO_6 octahedra and edges plus corners with the MoO_4 tetrahedra (Figure 2). The MoO_4 tetrahedra are slightly distorted with one Mo–O2 distance at 1.728(6) Å and three distances at 1.751(2) Å, while the BaO_6 octahedra have only one Ba–O1 distance at 2.781(2) Å but a significant degree of angle distortion. The cesium decahedra are very distorted with distances varying between 2.872(7) and 3.278(2) Å.

The bond distances are moreover compared in the Table 3 with the distances reported for the isotructural $K_2Ba(MoO_4)_2$[48] and $Rb_2Ba(MoO_4)_2$[46] compounds. One sees very clearly a trend of increasing alkali–oxygen bond distances in the 10-fold-coordinated AO_{10} polyhedra when the ionic radius of the alkali cation (K, Rb, Cs) increases down the series of the alkali metals (1.59, 1.66, and 1.81 Å for K, Rb, and Cs, respectively, in coordination [X], according to the tabulated data of Shannon[49]). The situation in $K_2Ba(MoO_4)_2$[48] is peculiar and is worth pointing out. Because of the similar ionic radii of Ba^{2+} and K^+, anti-site mixing occurs both on the 10-fold-coordinated site (88.78(17)% K and 11.22(17)% Ba) and the 6-fold-coordinated site (77.5(3)% Ba and 22.5(3)% K),[48] which corresponds to the chemical formula $(K_{0.888(2)}Ba_{0.112(2)})_2(Ba_{0.775(3)}K_{0.225(3)})(MoO_4)_2$. Anti-site mixing was not reported in $Rb_2Ba(MoO_4)_2$.[46] It was tested for

$Cs_2Ba(MoO_4)_2$, but the Rietveld refinement did not indicate its occurrence, as could be expected from the large difference in ionic radii between the Ba^{2+} and Cs^+ cations.

When looking at the Ba–O distances in the BaO_6 octahedra in this series of isotructural compounds, one observes very similar distances in $Cs_2Ba(MoO_4)_2$ and $Rb_2Ba(MoO_4)_2$[46] but a higher degree of angle distortion in the latter compound, as shown by the values of the bond angle variance. The expected average ionic radius in the "$Ba_{0.775(3)}K_{0.225(3)}O_6$" octahedra in $K_2Ba(MoO_4)_2$ is larger than those for the Rb and Cs compounds due to the anti-site mixing. But surprisingly at first sight, the average $Ba_{0.775(3)}K_{0.225(3)}$–O distance is shorter (2.735(4) Å). The degree of angle distortion is even higher than in the Rb and Cs compounds, however (as indicated again by the bond angle variance), which compensates for the K substitution and slightly higher average ionic radius of the 6-fold-coordinated cation.

Finally, the average Mo–O bond length in the MoO_4 tetrahedra is smaller in $Cs_2Ba(MoO_4)_2$ (1.745 Å) in comparison to $Rb_2Ba(MoO_4)_2$ (1.757 Å), showing that a compression of the MoO_4 tetrahedra occurs when the ionic radius of the alkali cation increases (and the volume of the alkali cation decahedra augments). The reported average Mo–O bond length in $K_2Ba(MoO_4)_2$ is very similar to that in $Cs_2Ba(MoO_4)_2$, but the angular distortion is much less.

To conclude this section on the structural characterization of $Cs_2Ba(MoO_4)_2$, the unit cell volume is compared with those reported for a series of isotructural compounds $A_2Ba(MO_4)_2$, with various transition-metal cations (M = Cr, Mo, W, Mn, V) and A alkali or alkaline-earth cations (A = K, Rb, Cs, Sr, Ba) (see Figures 3a,b). One sees a very clear linear increasing trend of the unit cell volume with increasing size of the A cation (Figure 3a). Three distinct trends are visible, with almost parallel slopes. The first group includes $Cs_2Ba(MoO_4)_2$ together with $Rb_2Ba(MoO_4)_2$,[46] $K_2Ba(MoO_4)_2$, and $Rb_2Ba(WO_4)_2$.[48] $Rb_2Ba(CrO_4)_2$[50] and $K_2Ba(CrO_4)_2$[48] form a separate group due to the much smaller ionic radius of hexavalent Cr in 4-fold coordination (0.26 Å) in comparison to hexavalent Mo (0.41 Å) and W (0.42 Å). Interestingly, the third class of compounds ($Sr_2Ba(CrO_4)_2$,[51] $Sr_2Ba(VO_4)_2$,[52] $Ba_3(MnO_4)_2$,[53] $Ba_3(CrO_4)_2$,[51] and $Ba_3(VO_4)_2$[52]), where A is now an alkaline earth (A = Sr, Ba) and the transition metal (M = V, Cr, Mn) is pentavalent, shows the same linear trend with an almost identical slope. The same classification appears on plotting the unit cell volume versus the normalized difference in ionic radius between the A cation and the M transition metal (see Figure 3b). The slope is positive and very similar between the different groups.

Finally, it is interesting to look at the relationship between the *a* and *c* lattice parameters in the palmierite structure.

Table 2. Refined Atomic Positions in $Cs_2Ba(MoO_4)_2$ Derived from the ND Refinement[a]

atom	oxidn state	Wyckoff	x	y	z	B_{eq} (Å^2)
O1	−2	18h	0.48877(15)	0.51123(15)	0.24536(9)	2.99(5)
Cs	+1	6c	0	0	0.19794(19)	1.80(8)
O2	−2	6c	0	0	0.32255(16)	6.7(2)
Mo	+6	6c	0	0	0.39754(14)	1.29(6)
Ba	+2	3a	0	0	0	2.4(1)

[a]$R_p = 10.0$, $R_{wp} = 10.5$, $R_{exp} = 2.83$, $\chi^2 = 13.7$. Individual B parameters: O1, $B_{11} = 1.96(5)$; $B_{22} = 1.96(5)$, $B_{33} = 5.1(1)$, $B_{12} = 1.24(6)$, $B_{13} = 0.40(3)$, $B_{23} = -0.40(3)$; Cs, $B_{11} = 1.9(1)$, $B_{22} = 1.9(1)$, $B_{33} = 1.6(2)$, $B_{12} = 0.9(6)$; O2, $B_{11} = 9.5(3)$, $B_{22} = 9.5(3)$, $B_{33} = 1.0(2)$, $B_{12} = 4.8(2)$; Mo, $B_{11} = 1.21(8)$, $B_{22} = 1.21(8)$, $B_{33} = 1.4(1)$, $B_{12} = 0.60(4)$; Ba, $B_{11} = 3.2(2)$, $B_{22} = 3.2(2)$, $B_{33} = 0.9(3)$, $B_{12} = 1.6(1)$.

Table 3. Bond Lengths in $Cs_2Ba(MoO_4)_2$ Obtained from the ND Refinement and Comparison with the Bond Distances in $K_2Ba(MoO_4)_2$[48] and $Rb_2Ba(MoO_4)_2$[46]

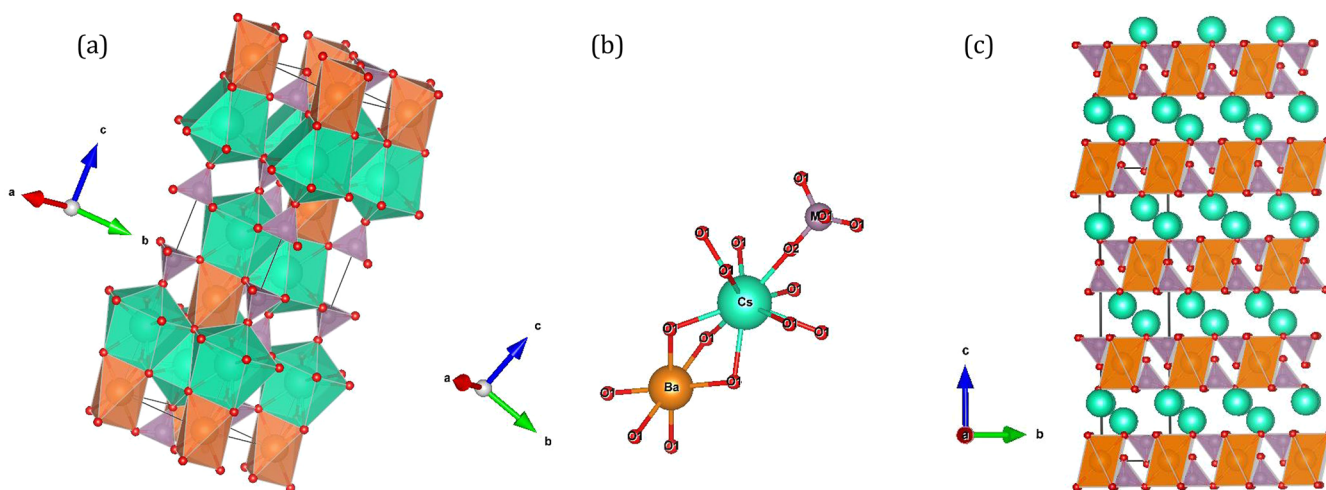| $Cs_2Ba(MoO_4)_2$ (this work)		$Rb_2Ba(MoO_4)_2$[46]		$K_2Ba(MoO_4)_2$[48]	
bond	bond length (Å)	bond	bond length (Å)	bond	bond length (Å)
Cs−O1 (×6)	3.278(2)	Rb−O1 (×6)	3.167(5)	K/Ba−O1 (×6)	3.0811(11)
Cs−O1 (×3)	3.169(5)	Rb−O1 (×3)	2.913(4)	K/Ba−O1 (×3)	2.761(4)
Cs−O2	2.872(7)	Rb−O2	2.772(7)	K/Ba−O2	2.637(7)
Ba−O1 (×6)	2.781(2)	Ba−O1 (×6)	2.783(4)	BaK-O1 (×6)	2.735(4)
Mo−O1 (×3)	1.751(2)	Mo−O1 (×3)	1.764(4)	Mo−O1 (×3)	1.750(4)
Mo−O2	1.728(6)	Mo−O2	1.739(7)	Mo−O2	1.726(7)

Figure 2. Crystal structure of $Cs_2Ba(MoO_4)_2$: (a) unit cell representation; (b) detailed view of the coordination environment of the cations; (c) extended view showing the layers in the ab plane. The MoO_4 tetrahedra are shown in purple, the BaO_6 octahedra in orange, the CsO_{10} decahedra in green, and the oxygen atoms in red.

Considering again the same isostructural compounds (Figure 3c), divided this time according to the nature of the A cation (A = K, Rb, Cs, Sr, Ba), one sees a negative trend between the a and c lattice parameters, with almost parallel slopes between the different classes. This observation was already made in the work of Chance et al.[48] and is extended here to a larger set of compounds. As the ionic radius of the metal M cation increases, the MO_4 tetrahedra expand, thus producing an increase in the a parameter. At the same time, the AO_{10} sites are compressed axially along the c direction (the axial A−O1 (×3) and A−O2 bonds along c shorten) and expand equatorially in the ab plane (the six A−O2 bonds lengthen) (see Figure 2), resulting in a decrease in the c lattice parameter. If $Cs_2Ba(WO_4)_2$ and $Cs_2Ba(CrO_4)_2$ exist as stable phases (their existences have not been reported to this date in the literature), their lattice parameters should fall on a parallel trend.

3.2. Assessment of the Thermal Expansion with Temperature. The thermal expansion of $Cs_2Ba(MoO_4)_2$ was assessed up to 673 K using high-temperature X-ray diffraction. No polymorphic transition was detected. The unit cell parameters derived from a Rietveld refinement of the XRD patterns at each measurement temperature are given in Table 4. The evolution of the relative thermal expansions of the a and c unit cell parameters, i.e. $(a − a_0)/a_0$ and $(c − c_0)/c_0$ (where a_0 and c_0 are the reference lengths at room temperature), is shown in Figure 4. The expansion is higher along the a and b directions, where MoO_4 tetrahedra alternate with BaO_6 octahedra via corner sharing, and is more limited along the c

direction, where bilayers of CsO_{10} dodecahedra make the linkages between the previous layers. The volumetric thermal expansion is equal to $\alpha_V \approx 43.0 \times 10^{-6}$ K^{-1} in the temperature range 298−673 K. The mean relative linear thermal expansion coefficient $(l − l_0)/l_0 = dl/l_0$, where $l = (abc)^{1/3}$, was moreover assessed and fitted as a polynomial function of the temperature T(K)
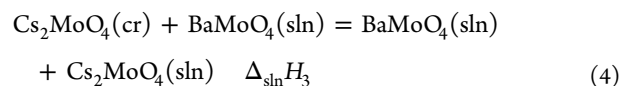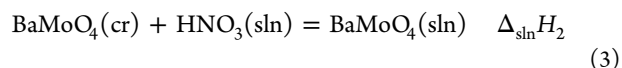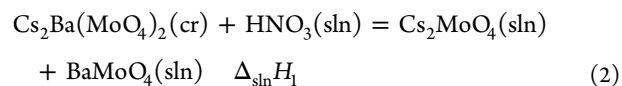
$$dl/l_0 = -6.94 \times 10^{-3} + 2.16789 \times 10^{-5}T$$
$$+ 5.38893 \times 10^{-9}T^2 \tag{1}$$

where $l_0 = (a_0b_0c_0)^{1/3}$ is the reference length at room temperature.

The relative thermal expansion is found between those reported in the literature for Cs_2MoO_4[23] and $BaMoO_4$[54] (shown as dotted lines in Figure 4).

3.3. Standard Enthalpy of Formation Determination. The enthalpy of formation of $Cs_2Ba(MoO_4)_2$ was measured using the thermochemical cycle detailed in Table 5 in a solution of 2 M HNO_3. The corresponding reaction scheme is

$$Cs_2Ba(MoO_4)_2(cr) + HNO_3(sln) = Cs_2MoO_4(sln)$$
$$+ BaMoO_4(sln) \quad \Delta_{sln}H_1 \tag{2}$$

$$BaMoO_4(cr) + HNO_3(sln) = BaMoO_4(sln) \quad \Delta_{sln}H_2 \tag{3}$$

$$Cs_2MoO_4(cr) + BaMoO_4(sln) = BaMoO_4(sln)$$
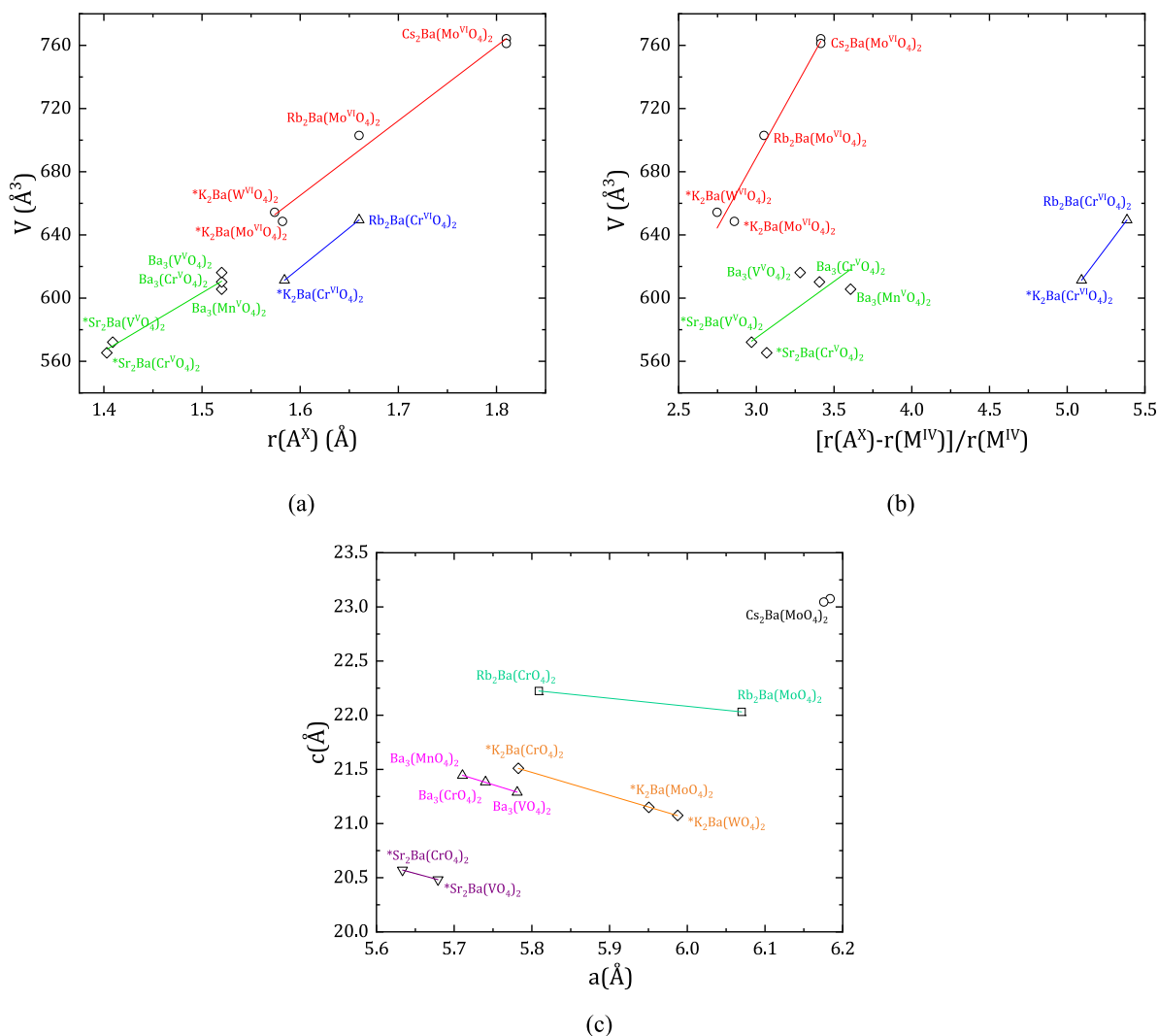$$+ Cs_2MoO_4(sln) \quad \Delta_{sln}H_3 \tag{4}$$

(a)

(b)

(c)

Figure 3. Evolution of the unit cell volume of $A_2Ba(MO_4)_2$ with A = K, Rb, Cs, Sr, Ba and M = Cr, Mo, W, Mn, V as a function of the (a) ionic radius of the A cation in 10-fold coordination and (b) difference in ionic radis between the A cation and the M transition-metal element. (c) Relationship between the a and c lattice parameters in several classes of $A_2Ba(MO_4)_2$ compounds.

Table 4. Refined Unit Cell Parameters and Unit Cell Volume as a Function of Temperature

T (K)	a (Å)	c (Å)	V (Å^3)
298	6.184(2)	23.081(8)	764.4(4)
373	6.196(2)	23.106(8)	768.1(4)
473	6.203(2)	23.124(9)	770.6(5)
573	6.212(3)	23.14(1)	773.4(6)
673	6.224(2)	23.169(8)	777.3(5)

The dissolutions of $Cs_2Ba(MoO_4)_2$, $BaMoO_4$, and Cs_2MoO_4 in the nitric acid solutions were in all cases instantaneous. The details of all calorimetric results are given in Table 6.

By adjusting the amount of dissolved samples such that sol.1 (with associated dissolution enthalpy $\Delta_{sln}H_1$) and sol.3 (with associated dissolution enthalpy $\Delta_{sln}H_3$) had the same final composition, one can express the enthalpy of the reaction of formation from the constituting ternary oxides (eq 5) as

$$\Delta_r H_m° = \Delta_{sln}H_2 + \Delta_{sln}H_3 - \Delta_{sln}H_1 = -5.14 \pm 2.71 \text{ kJ mol}^{-1}.$$

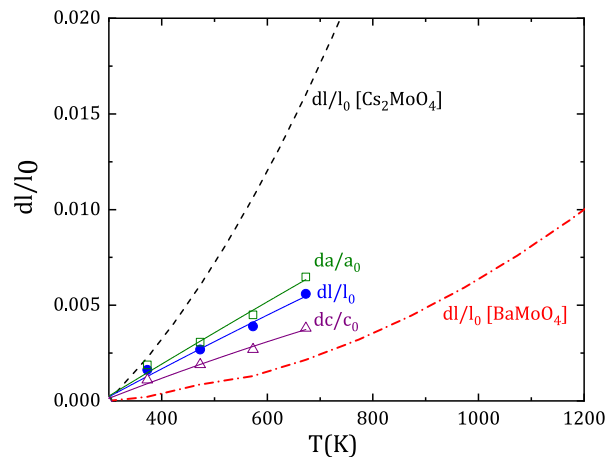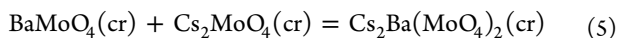$$BaMoO_4(cr) + Cs_2MoO_4(cr) = Cs_2Ba(MoO_4)_2(cr) \quad (5)$$

Figure 4. Relative linear thermal expansion of $Cs_2Ba(MoO_4)_2$ along the crystallographic axes. Also shown (as dotted line) are the results of Wallez et al.[23] and Sahu et al.[54] for the mean relative linear expansions dl/l_0 of Cs_2MoO_4 and $BaMoO_4$, respectively.

**Table 5. Thermochemical Cycle Used to Determine the Standard Enthalpy of Formation of $Cs_2Ba(MoO_4)_2$**[a]

entry	reaction	$\Delta_{sln}H$(298.15 K) (kJ mol^{-1})	ref
1	$Cs_2Ba(MoO_4)_2$(cr) + (sln) = $BaMoO_4$(sln) + Cs_2MoO_4(sln)	-87.55 ± 1.48[b]	this work
2	$BaMoO_4$(cr) + (sln) = $BaMoO_4$(sln)	-34.37 ± 0.34[b]	this work
3	Cs_2MoO_4(cr) + $BaMoO_4$(sln) = $BaMoO_4$(sln) + Cs_2MoO_4(sln)	-58.32 ± 2.24[b]	this work

entry	reaction	$\Delta_f H_m°$(298.15 K) (kJ mol^{-1})	ref
4	Ba(cr) + Mo(cr) + 2O_2(g) = $BaMoO_4$(cr)	-1547.23 ± 1.22	56
5	2Cs(cr) + Mo(cr) + 2O_2(g) = Cs_2MoO_4(cr)	-1514.25 ± 0.72[c]	36–38, 55
6	2Cs(cr) + Ba(cr) + 2Mo(cr) + 4O_2(g) = $Cs_2Ba(MoO_4)_2$(cr)	-3066.6 ± 3.1	this work

[a]Measurements were performed in the temperature interval T = 298.15 ± 0.30 K. The enthalpy of formation of $Cs_2Ba(MoO_4)_2$ was calculated using the relation $\Delta_f H_m°(6) = \Delta_{sln}H(2) + \Delta_{sln}H(3) - \Delta_{sln}H(1) + \Delta_f H_m°(4) + \Delta_f H_m°(5)$. [b]Expanded uncertainty U with a coverage factor k = 2, corresponding to a 95% confidence interval. [c]The selected value is the average of the data reported in refs 36–38 and 55.

Table 6. Measured Dissolution Enthalpies at 298.15 K for $Cs_2Ba(MoO_4)_2$(cr) (M = 723.042 g mol^{-1}), $BaMoO_4$ (M = 297.276 g mol^{-1}), and Cs_2MoO_4 (M = 425.766 g mol^{-1}) in 2 M HNO_3[a]

entry	$m(Cs_2Ba(MoO_4)_2)$ (mg)	ΔT (mK)	C_p (J K^{-1})	Q (J)	$\Delta_r H_m°$(298.15 K) (kJ mol^{-1})
1	71.81	79.932	109.888	−8.78	−88.44
2	73.17	80.361	110.123	−8.85	−87.45
3	72.25	78.965	110.271	−8.71	−87.14
4	72.30	78.639	110.118	−8.66	−86.60
5	72.25	79.972	110.112	−8.81	−88.12

entry	$m(BaMoO_4)$ (mg)	ΔT (mK)	C_p (J K^{-1})	Q (mJ)	$\Delta_r H_m°$(298.15 K) (kJ mol^{-1})
1	42.43	44.682	110.166	−4922.44	−34.49
2	42.39	44.656	110.382	−4929.22	−34.57
3	42.55	44.454	110.255	−4901.28	−34.24
4	42.35	44.474	110.194	−4900.77	−34.40
5	42.62	44.455	110.160	−4897.16	−34.16

entry	$m(Cs_2MoO_4)$ (mg)	ΔT (mK)	C_p (J K^{-1})	Q (J)	$\Delta_r H_m°$(298.15 K) (kJ mol^{-1})
1	29.64	37.353	109.520	−4.09	−58.76
2	29.82	37.021	109.544	−4.06	−57.90
3	29.74	38.171	109.738	−4.19	−59.97
4	29.67	36.234	109.555	−3.97	−56.96
5	29.65	36.895	109.481	−4.04	−58.00

[a]The measurements were performed in the temperature range T = 298.15 ± 0.30 K. Definitions: m, sample weight; ΔT, temperature change caused by the dissolution; C_p, energy equivalent of the calorimeter; Q, amount of heat generated by the dissolution; $\Delta_r H_m°$(298.15 K), molar enthalpy of the reaction.
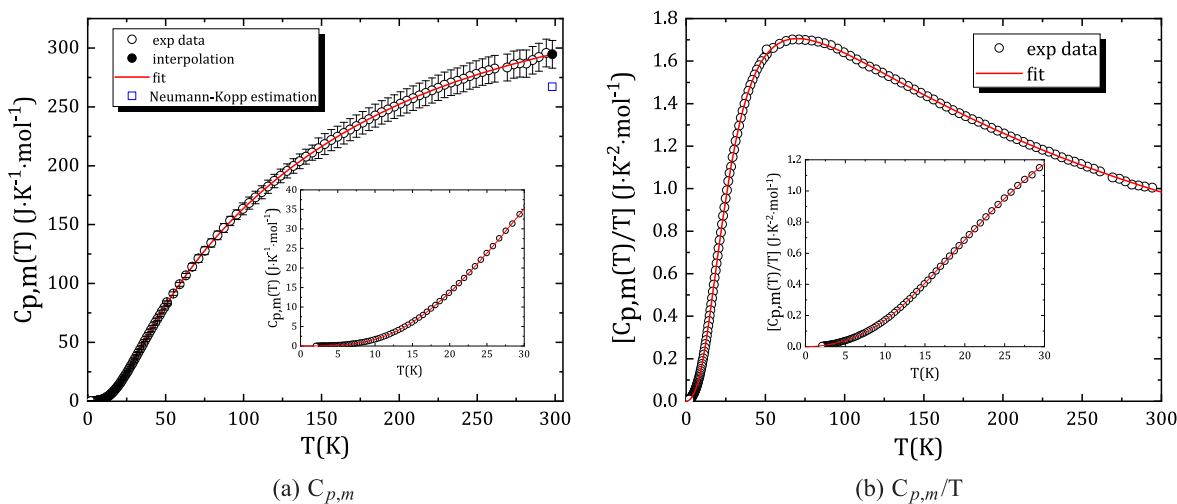
Figure 5. Heat capacity of $Cs_2Ba(MoO_4)_2$ (○) and fit to the data (red line): (a) $C_{p,m}$; (b) $C_{p,m}/T$.

When the aforementioned enthalpy of reaction is combined with the enthalpies of formation of Cs_2MoO_4(cr) and $BaMoO_4$(cr), the standard enthalpy of formation of $Cs_2Ba(MoO_4)_2$(cr) is finally derived as $\Delta_f H_m°$($Cs_2Ba(MoO_4)_2$, cr,

298.15 K) = -3066.6 ± 3.1 kJ mol^{-1}. The selected value for the enthalpy of formation of Cs_2MoO_4(cr) is the average of the data reported by O'Hare and Hoekstra[37] and revised by Cordfunke and Konings[38] (-1514.5 ± 1.0 kJ mol^{-1}), the data

Table 7. Fitting Parameters of the Heat Capacity of $Cs_2Ba(MoO_4)_2$ within the Temperature Intervals $T = 2.1-16.9$ K and $T = 14.4-294.3$ K

harmonic lattice model		Debye and Einstein fit	
temp range (K)	2.1–16.9	temp range (K)	14.4–294.3
γ (mJ mol^{-1} K^{-2})	0	n_D (mol)	4.3802
B_3 (mJ mol^{-1} K^{-4})	1.48	θ_D (K)	166.36
B_5 (mJ mol^{-1} K^{-6})	2.91387×10^{-3}	n_{E1} (mol)	3.0006
B_7 (mJ mol^{-1} K^{-8})	-6.40657×10^{-6}	θ_{E1} (K)	243.08
		n_{E2} (mol)	3.7308
		θ_{E2} (K)	456.77
		n_{E3} (mol)	3.0908
		θ_{E3} (K)	873.98
		$n_D + n_{E1} + n_{E2} + n_{E3}$ (mol)	14.2

reported by Smith et al.[36] (-1514.69 ± 1.54 kJ mol^{-1}) and by Benigni et al.[55] (-1513.56 ± 1.11 kJ mol^{-1}). The enthalpy of formation of $BaMoO_4$ was taken from the critical review of Gamsjäger and Morishita,[56] on the basis of the data measured by O'Hare[57] and Shukla et al.[58]

3.4. Standard Entropy Determination by Low-Temperature Calorimetry. The low-temperature heat capacity data collected in the temperature range $T = 2.1-294.3$ K are shown in Figure 5a and given in Table S1 in the Supporting Information. The heat capacity of $Cs_2Ba(MoO_4)_2$ shows a smooth increase with temperature, reaching values of $\sim$30 J K^{-1} mol^{-1} below the classical Dulong−Petit limit ($C_{lat} = 3nR \approx 324$ J K^{-1} mol^{-1}) toward 298.15 K.

The heat capacity and standard entropy at 298.15 K of $BaCs_2(MoO_4)_2$ were obtained by fitting the experimental data using a harmonic-lattice model[59] below $T = 16.9$ K and a combination of one Debye and three Einstein heat capacity functions[60−62] for $T = 14.4-294.3$ K. The Levenberg−Marquardt iteration algorithm implemented in the OriginPro 2019 software was used for the fitting, using Origin C type fitting functions in the high-temperature region and simple expression type functions in the low-temperature region. The fitted data are shown with solid lines in Figure 5. A slight scatter in the experimental data is seen around 270−300 K related to a vitreous transition of the thermal grease around 300 K, which is unfortunately not reproducible from one experiment to the other. The fitted heat capacity function increases smoothly in this temperature region and follows a reasonable trend.

A harmonic-lattice model[59] was used in the low-temperature region to represent the phonon contribution, as given by eq 6. Generally, the number of required terms increases with the high temperature limit of the fit:

$$C_{latt} = \sum B_n T^n \quad n = 3, 5, 7, 9, \ldots \tag{6}$$

The fitting coefficients are given in Table 7. The electronic contribution of the conduction electrons at the Fermi surface are expressed with the linear term γT.[63] It was found to be equal to zero in this case, as expected for such an insulating material.

In the high-temperature region, the contribution from lattice vibrations prevails, which is modeled herein using a combination of Debye and Einstein functions,[64] as expressed in eq 7.

$$C_{p,m} = n_D D(\theta_D) + n_{E1} E(\theta_{E1}) + n_{E2} E(\theta_{E2}) + n_{E3} E(\theta_{E3}) \tag{7}$$

where $D(\theta_D)$, $E(\theta_{E1})$, $E(\theta_{E2})$, and $E(\theta_{E3})$ are the Debye and Einstein functions, respectively, as written in eqs 8 and 9. θ_D, θ_{E1}, θ_{E2} and θ_{E3} are the characteristic Debye and Einstein temperatures. n_D, n_{E1}, n_{E2}m and n_{E3} are adjustable parameters, whose sum ($n_D + n_{E1} + n_{E2} + n_{E3}$) should come close to the number of atoms in the formula unit:

$$D(\theta_D) = 9R \left(\frac{T}{\theta_D}\right)^3 \int_0^{\theta_D/T} \frac{e^x x^4}{[e^x - 1]^2} \, dx \tag{8}$$

$$E(\theta_E) = 3Rx^2 \frac{e^x}{[e^x - 1]^2} \quad x = \frac{\theta_E}{T} \tag{9}$$

where R is the universal gas constant and is equal to 8.3144598 J K^{-1} mol^{-1}.

This method has been used in the literature for various inorganic materials: the iron phosphates $Fe(PO_3)_3$, $Fe_2P_2O_7$, $FePO_4$, $Fe_3(P_2O_7)_2$, Fe_3PO_7 and $Fe_4(P_2O_7)_3$,[65−67] zirconolite $CaZrTi_2O_7$,[60] calcium titanate $CaTiO_3$,[61] dicesium molybdate $Cs_2Mo_2O_7$,[68] the mixed cesium sodium molybdate $Cs_3Na(MoO_4)_2$,[36] sodium uranate Na_4UO_5 and sodium neptunate Na_4NpO_5,[69] and potassium uranate K_2UO_4 and potassium neptunate K_2NpO_4.[70] Three Einstein functions were used in combination with a Debye function. The fitted parameters are given in Table 7. The deviation of the fitted data from the experimental results is below 0.4% above $\sim$10 K (see Figure 6). The sum $n_D + n_{E1} + n_{E2} + n_{E3}$ is equal to 14.2 and is hence a
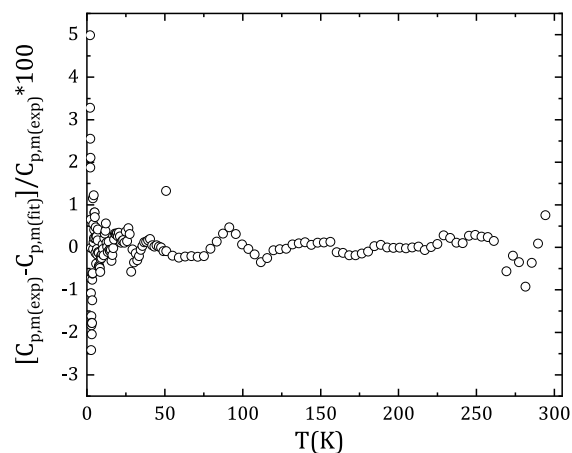

Figure 6. Deviation of the fitting equations from the experimental data.

Table 8. Thermodynamic Data for $Cs_2Ba(MoO_4)_2$ at Pressure p = 100 kPa

reaction	$\Delta_r H_m°$(298.15 K) (kJ mol^{-1})	$\Delta_r S_m°$(298.15 K) (J K^{-1} mol^{-1})	$\Delta_r G_m°$(298.15 K) (kJ mol^{-1})
$2Cs(cr) + Ba(cr) + 2Mo(cr) + 4O_2(g) = Cs_2Ba(MoO_4)_2(cr)$	-3066.6 ± 3.1	-729.4 ± 11.9	-2849.1 ± 4.7
$Cs_2O(cr) + BaO(cr) + 2MoO_3(cr) = Cs_2Ba(MoO_4)_2(cr)$	-682.5 ± 4.6	8.8 ± 12.2	-685.1 ± 5.9
$Cs_2MoO_4(cr) + BaMoO_4(cr) = Cs_2Ba(MoO_4)_2(cr)$	-5.1 ± 3.4	-19.8 ± 12.0	0.8 ± 4.9

slight overestimation, in comparison to the expected 13 atoms per formula unit. The derived heat capacity value at 298.15 K is also about 27 J K^{-1} mol^{-1} higher than that predicted from the Neumann−Kopp rule applied to {$BaMoO_4$[71] + Cs_2MoO_4[38,72]} (267.1 J K^{-1} mol^{-1}) (see Figure 5a). The occurrence of a structural disorder in the material by, for instance, mutual substitution of the Cs and Ba cations (anti-site mixing) that would contribute to an excess entropic contribution was considered but discarded on the basis of the collected neutron diffraction data as outlined in section 3.1. The presence of a secondary (impurity) phase can also be ruled out on the basis of the collected XRD and ND data. Moreover, a lower heat capacity value at 298.15 K, and thus lower standard entropy at 298.15 K in comparison to that reported herein, would mean that the quaternary phase $Cs_2Ba(MoO_4)_2$ is not stable at room temperature and rather disproportionates into {$BaMoO_4$ + Cs_2MoO_4}, as indicated by the equilibrium thermochemical calculations detailed hereafter. This is not in accordance with the present experimental observations; hence, the collected data seem to be reliable, despite the overestimated fitted value for the number of atoms and the difference from the Neumann−Kopp approximation. Nevertheless, it would be beneficial to repeat the measurement on a larger amount of material for confirmation of the present results.

The heat capacity value obtained at 298.15 K by interpolation is $C_{p,m}°(Cs_2Ba(MoO_4)_2$, cr, 298.15 K) = 294.6 $\pm$ 11.8 J K^{-1} mol^{-1}. The standard entropy at 298.15 K determined by numerical integration of $C_{p,m}/T = f(T)$ with the aforementioned functions, using T = 16.5 K as the conjunction temperature, is $S_m°(Cs_2Ba(MoO_4)_2$, cr, 298.15 K) = 381.2 $\pm$ 11.8 J K^{-1} mol^{-1}. Standard thermodynamic functions were also derived for selected temperatures for T = 0−300 K and are given in Table S2 in the Supporting Information.

When the standard entropy value of the quaternary compound is combined with those for cesium,[73] barium,[73] molybdenum,[38] and oxygen,[73] the standard entropy of formation of $Cs_2Ba(MoO_4)_2$ is derived as $\Delta_f S_m°(Cs_2Ba(MoO_4)_2$, cr, 298.15 K) = -729.4 ± 11.9 J K^{-1} mol^{-1}. From the measured enthalpy of formation and standard enthalpy of formation, the Gibbs energy of formation at 298.15 K was determined as $\Delta_f G_m°(Cs_2Ba(MoO_4)_2$, cr, 298.15 K) = -2849.1 ± 4.7 kJ mol^{-1}.

The entropy, enthalpy, and Gibbs energy of formation of $Cs_2Ba(MoO_4)_2$ from its constituting oxides were finally derived as given in Table 8. These data were calculated using the following values for the enthalpies of formation of $Cs_2O(cr)$, $BaO(cr)$, $MoO_3(cr)$, $BaMoO_4(cr)$ and $Cs_2MoO_4(cr)$, respectively: -345.98 ± 1.17,[38] -548.1 ± 2.5,[74] -745.0 ± 1.0,[38] -1547.23 ± 1.22,[56] and -1514.25 ± 0.72[36,37,55,78] kJ mol^{-1}. The corresponding standard entropies are 146.87 ± 0.44,[38] 70.01 ± 0.10,[75] 77.76 ± 1.30,[38] 152.69 ± 1.53,[71] and 248.35 ± 0.30[38,72] J K^{-1} mol^{-1}.

The derived Gibbs energy of formation of $Cs_2Ba(MoO_4)_2$ from the constituting binary oxides $Cs_2O(cr)$, $BaO(cr)$, and $MoO_3(cr)$ equals $\Delta_f G_{m,bin.ox.}°$(298.15 K) = -685.1 ± 5.9 kJ

mol^{-1}. The Gibbs energy of formation from the constituting ternary oxides $Cs_2MoO_4(cr)$ and $BaMoO_4(cr)$ is slightly positive at 298.15 K: $\Delta_f G_{m,ter.ox.}°$(298.15 K) = 0.8 ± 4.9 kJ mol^{-1}, suggesting that $Cs_2Ba(MoO_4)_2$ is not stable with respect to $Cs_2MoO_4(cr)$ and $BaMoO_4(cr)$ at room temperature.

Interestingly, a similar result was obtained for $Cs_3Na(MoO_4)_2$ formed by a stoichiometric reaction between Cs_2MoO_4 and Na_2MoO_4, as reported by Smith et al.[36] The Gibbs energy of formation from the constituting ternary oxides was found to be slightly positive at 298.15 K: i.e., 2.3 ± 4.4 kJ mol^{-1}. It was shown, however, that the Gibbs energy of reaction becomes negative above T = 440 K, in good accordance with the experimental observations of Zolotova et al.[76] and Smith et al.[36] with respect to the synthesis conditions (interaction noticed by XRD above 523 K and need for long thermal treatments). In the case of $Cs_2Ba(MoO_4)_2$, the Gibbs energy of reaction from the ternary oxides is slightly positive but becomes negative when the entropy of the quaternary phase is increased to 393.0 J K^{-1} mol^{-1} (yielding -2.72 kJ mol^{-1}) or when the enthalpy of formation is set to -3069.7 kJ mol^{-1} (yielding -2.30 kJ mol^{-1}), which are values within the uncertainty ranges of the calorimetric measurements. This result is also in good accordance with preliminary results obtained by differential scanning calorimetry on $Cs_2Ba(MoO_4)_2$, which indicate an incongruent melting above ~1150 K and a decomposition into Cs_2MoO_4 and $BaMoO_4$ during cooling, as evidenced from post-XRD characterizations. The latter data will be presented in future works.

4. CONCLUSIONS

With the aim of improving the assessment of the source term in severe accident codes, the solubility of cesium in $BaMoO_4$ was investigated by our research group, which suggested a very limited solubility but revealed instead the formation of the quaternary phase $Cs_2Ba(MoO_4)_2$ by the reaction between $BaMoO_4$ and Cs_2MoO_4 at high temperature. This novel double molybdate adopts a palmierite type of structure, as confirmed from the XRD and ND results. The compound's thermal expansion was evaluated between room temperature and 673 K, which yielded a volumetric thermal expansion coefficient equal to $\alpha_V \approx 43.0 \times 10^{-6}$ K^{-1}. Its standard enthalpy of formation was assessed using solution calorimetry as $\Delta_f H_m°(Cs_2Ba(MoO_4)_2$, cr, 298.15 K) = -3066.6 ± 3.1 kJ mol^{-1}, and its standard entropy was derived from low-temperature thermal relaxation calorimetry as $S_m°(Cs_2Ba(MoO_4)_2$, cr, 298.15 K) = 381.2 ± 11.8 J K^{-1} mol^{-1}.

These findings could be of interest for the field of photoluminescent materials and have implications for the safety assessment of irradiated fuel behavior. The existence of this phase is particularly relevant for the fuel chemistry in fast neutron reactors, where higher burnup and oxygen potentials are reached. Because Cs_2MoO_4 is largely dominant in the JOG between the fuel and cladding and the presence of barium has also been identified in this layer, one could imagine a possible formation of $Cs_2Ba(MoO_4)_2$ in localized areas. To test this

hypothesis, a complete thermodynamic assessment of the Cs−Ba−Mo−O system using the CALPHAD methodology would be required, allowing the performance of thermodynamic equilibrium calculations under various oxygen potential and temperature conditions. The thermodynamic data collected herein, i.e. standard enthalpy of formation and standard entropy, can serve as inputs for the development of such a thermodynamic model of the complex multi-element JOG system.

■ ASSOCIATED CONTENT

Ⓢ Supporting Information

The Supporting Information is available free of charge at https://pubs.acs.org/doi/10.1021/acs.inorgchem.0c01469.

> Experimental heat capacity data of $Cs_2Ba(MoO_4)_2$ and standard thermodynamic functions from 0 to 300 K (PDF)

Accession Codes

CCDC 2004804 contains the supplementary crystallographic data for this paper. These data can be obtained free of charge via www.ccdc.cam.ac.uk/data_request/cif, or by emailing data_request@ccdc.cam.ac.uk, or by contacting The Cambridge Crystallographic Data Centre, 12 Union Road, Cambridge CB2 1EZ, UK; fax: +44 1223 336033.

■ AUTHOR INFORMATION

Corresponding Author

    Anna L. Smith − *Delft University of Technology, Faculty of Applied Sciences, Radiation Science and Technology Department, 2629 JB Delft, The Netherlands;* Ⓞ orcid.org/0000-0002-0355-5859; Email: a.l.smith@tudelft.nl

Authors

    Nathan de Zoete − *Delft University of Technology, Faculty of Applied Sciences, Radiation Science and Technology Department, 2629 JB Delft, The Netherlands*
    Maikel Rutten − *Delft University of Technology, Faculty of Applied Sciences, Radiation Science and Technology Department, 2629 JB Delft, The Netherlands*
    Lambert van Eijck − *Delft University of Technology, Faculty of Applied Sciences, Radiation Science and Technology Department, 2629 JB Delft, The Netherlands*
    Jean-Christophe Griveau − *Joint-Research Centre Karlsruhe, European Commission, D-76125 Karlsruhe, Germany*
    Eric Colineau − *Joint-Research Centre Karlsruhe, European Commission, D-76125 Karlsruhe, Germany*

Complete contact information is available at:
https://pubs.acs.org/10.1021/acs.inorgchem.0c01469

Notes

The authors declare no competing financial interest.

■ REFERENCES

(1) Yoon, J.-W.; Ryu, J. H.; Shim, K. B. Photluminescence in nanocrystalline $MMoO_4$ (M = Ca, Ba) synthesized by a polymerized complex method. *Mater. Sci. Eng., B* **2006**, *127*, 154−158.

(2) Lei, M.; Ye, C. X.; Ding, S. S.; Bi, K.; Xiao, H.; Sun, Z. B.; Fan, D. Y.; Yang, H. J.; Wang, Y. G. Controllable route to barium molybdate crystal and their photoluminescence. *J. Alloys Compd.* **2015**, *639*, 102−105.

(3) Sorokin, N. I. Ionic conductivity of double sodium-scandium and cesium-zirconium molybdates. *Phys. Solid State* **2009**, *51*, 1128−1130.

(4) Voronkova, V.I.; Leonidov, I.A.; Kharitonova, E.P.; Belov, D.A.; Patrakeev, M.V.; Leonidova, O.N.; Kozhevnikov, V.L. Oxygen ion and electron conductivity in fluorite-like molybdates $Nd_5Mo_3O_{16}$ and $Pr_5Mo_3O_{16}$. *J. Alloys Compd.* **2014**, *615*, 395−400.

(5) Sleight, A. W.; Brixner, L. H. A new ferroelastic transition in some $A_2(MO_4)_3$ molybdates and tungstates. *J. Solid State Chem.* **1973**, *7*, 172−174.

(6) Isupov, V. A. Binary Molybdates and Tungstates of Mono and Trivalent Elements as Possible Ferroelastics and Ferroelectrics. *Ferroelectrics* **2005**, *321*, 63−90.

(7) Kato, A.; Oishi, S.; Shishido, T.; Yamazaki, M.; Iida, S. Evaluation of stoichiometric rare-earth molybdate and tungstate compounds as laser materials. *J. Phys. Chem. Solids* **2005**, *66*, 2079−2081.

(8) Zharikov, E. V.; Zaldo, C.; Diaz, F. Double Tungstate and Molybdate Crystals for Laser and Nonlinear Optical Applications. *MRS Bull.* **2009**, *34*, 271−276.

(9) Tissot, R. G.; Rodriguez, M. A.; Sipola, D. L.; Voigt, J. A. X-ray powder diffraction study of synthetic palmierite, $K_2Pb(SO_4)_2$. *Powder Diffr.* **2001**, *16*, 92−97.

(10) Brillant, G. Interpretation and modelling of fission product Ba and Mo releases from fuel. *J. Nucl. Mater.* **2010**, *397*, 40−47.

(11) Imoto, S. Chemical state of fission products in irradiated UO_2. *J. Nucl. Mater.* **1986**, *140*, 19−27.

(12) Cordfunke, E. H. P.; Konings, R. J. M. Chemical interactions in water-cooled nuclear fuel: a thermochemical approach. *J. Nucl. Mater.* **1988**, *152*, 301−309.

(13) Cordfunke, E. H. P.; Konings, R. J. M. The release of fission products from degraded UO_2 fuel: Thermochemical aspects. *J. Nucl. Mater.* **1993**, *201*, 57−69.

(14) Tourasse, M.; Boidron, M.; Pasquet, B. Fission product behaviour in Phenix fuel pins at high burn-up. *J. Nucl. Mater.* **1992**, *188*, 49−57.

(15) Dumas, J.-C. *Etude des conditions de formation du Joint-Oxyde-Gaine dans les combustibles oxydes mixtes des reacteurs à neutrons rapides, observations et proposition d'un modèle de comportement des produits de fission volatils.* Ph.D. thesis, Institut national polytechnique de Grenoble, Grenoble, France, 1995.

(16) Maeda, K.; Asaga, T. Change of fuel-to-cladding gap width with the burn-up in FBR MOX fuel irradiated to high burn-up. *J. Nucl. Mater.* **2004**, *327*, 1−10.

(17) Thi, T. N. P. Caractérisation et modélisation du comportement thermodynamique du combustible RNR-Na sous irradiation. Ph.D. thesis, Ecole Doctorale Physique et Sciences de la Matière (Aix-Marseille University), 2014.

(18) Parrish, R.; Winston, A.; Harp, J.; Aitkaliyeva, A. TEM characterization of high burnup fast-reactor MOX fuel. *J. Nucl. Mater.* **2019**, *527*, 151794.

(19) Samuelsson, K.; Dumas, J.-C.; Sundman, B.; Lamontagne, J.; Gueneau, C. Simulation of the chemical state of high burnup $(U,Pu)O_2$ fuel in fast reactors based on thermodynamic calculations. *J. Nucl. Mater.* **2020**, *532*, 151969.

(20) Cappia, F.; Miller, B. D.; Aguiar, J. A.; He, L.; Murray, D. J.; Frickey, B. J.; Stanek, J. D.; Harp, J. M. Electron microscopy characterization of fast reactor MOX Joint Oxide-Gaine (JOG). *J. Nucl. Mater.* **2020**, *531*, 151964.

(21) Ishii, T.; Mizuno, T. Thermal conductivity of cesium molybdate Cs_2MoO_4. *J. Nucl. Mater.* **1996**, *231*, 242−244.

(22) Minato, K.; Takano, M.; Fukuda, K.; Sato, S.; Ohashi, H. Thermal expansion and thermal conductivity of cesium molybdate. *J. Alloys Compd.* **1997**, *255*, 18−23.

(23) Wallez, G.; Raison, P. E.; Smith, A. L.; Clavier, N.; Dacheux, N. High-temperature behavior of dicesium molybdate Cs_2MoO_4: Implications for fast neutron reactors. *J. Solid State Chem.* **2014**, *215*, 225−230.

(24) Kleykamp, H. The chemical state of the fission products in oxide fuels. *J. Nucl. Mater.* **1985**, *131*, 221−246.

(25) Barrachin, M.; Gavillet, D.; Dubourg, R.; Bremaecker, A. D. Fuel and fission product behaviour in early phases of a severe accident. Part I: Experimental results of the PHEBUS FPT2 test. *J. Nucl. Mater.* **2014**, *453*, 340−354.

(26) Kurosaki, K.; Tanaka, K.; Osaka, M.; Ohishi, Y.; Muta, H.; Uno, M.; Yamanaka, S. Chemical States of Fission Products and Actinides in Irradiated Oxide Fuels Analysed by Thermodynamic Calculation and Post-Irradiation Examination. *Progress in Nuclear Science and Technology* **2011**, *2*, 5−8.

(27) Paschol, J. O. A.; Kleykamp, H.; Thummler, F. Phase equilibria in the pseudoquaternary $BaO-UO_2-ZrO_2-MoO_2$ system. *J. Nucl. Mater.* **1987**, *151*, 10−21.

(28) Muromura, T.; Adachi, T.; Takeishi, H.; Yoshida, Z.; Yamamoto, T.; Ueno, K. Metallic phases precipitated in UO_2 fuel I. Phases in simulated fuel. *J. Nucl. Mater.* **1988**, *151*, 327−333.

(29) *Thermodynamic Characterisation of Fuel Debris and Fission Products Based on Scenario Analysis of Severe Accident Progression at Fukushima-Daiichi Nuclear Power Station*; www.oecd-nea.org/science/tcoff/.

(30) Rodriguez-Carvajal, J. Recent advances in magnetic structure determination by neutron powder diffraction. *Phys. B* **1993**, *192*, 55−69.

(31) van Eijck, L.; Cussen, L. D.; Sykora, G. J.; Schooneveld, E. M.; Rhodes, N. J.; van Well, A. A.; Pappas, C. Design and performance of a novel neutron powder diffractometer: PEARL at TU Delft. *J. Appl. Crystallogr.* **2016**, *49*, 1398−1401.

(32) Uriano, G. A. *National Bureau of Standards Certificate, Standard Reference Material 1655, Potassium Chloride KCl(cr) for Solution Calorimetry*; 1981.

(33) Parker, V. B. *Thermal Properties of Uni-univalent Electrolytes*; Government Printing Office: 1965.

(34) Wadsö, I.; Goldberg, R. N. Standards in Isothermal Microcalorimetry (IUPAC Technical Report). *Pure Appl. Chem.* **2001**, *73*, 1625−1639.

(35) Wagman, D. D.; Evans, W. H.; Parker, V. B.; Schumm, R. H.; Halow, I.; Bailey, S. M.; Churney, K. L.; Nuttall, R. L. The NBS tables of Chemical Thermodynamic Properties, Selected values for inorganic and C1 and C2 substances in SI units, NBS Washington, DC20234. *J. Phys. Chem. Ref. Data* **1982**, *11.1*

(36) Smith, A. L.; Pignié, M.-C.; van Eijck, L.; Griveau, J.-C.; Colineau, E.; Konings, R. J. M. Thermodynamic study of $Cs_3Na-(MoO_4)_2$: Determination of the standard enthalpy of formation and standard entropy at 298.15 K. *J. Chem. Thermodyn.* **2018**, *120*, 205−216.

(37) O'Hare, P. A. G.; Hoekstra, H. R. Thermochemistry of molybdates. I. Standard enthalpy of formation of cesium molybdate (Cs_2MoO_4). *J. Chem. Thermodyn.* **1973**, *5*, 851−856.

(38) Cordfunke, E. H. P.; Konings, R. J. M. *Thermochemical data for reactor materials and fission products; Thermochemical data for reactor materials and fission products*; Elsevier Science: 1990.

(39) Graham, R. L.; Hepler, L. Heats of Formation of Sodium Molybdate, Molybdic Acid and Aqueous Molybdate Ion. *J. Am. Chem. Soc.* **1956**, *78*, 4846.

(40) Koehler, M. F.; Pankratz, L. B.; Barany, R. *Sodium molybdates; heats of formation*; University of Michigan: 1962; p 5973.

(41) Tangri, R. P.; Venugopal, V.; Bose, D. K. Standard molar enthalpies of formation of sodium molybdates ($Na_2Mo_nO_{3n+1}$ with n = 1, 2, 3 or 4) at 298.15 K by solution calorimetry. *Thermochim. Acta* **1992**, *198*, 259−265.

(42) Taylor, B. N.; Kuyatt, C. E. *Guidelines for Evaluating and Expressing the Uncertainty of NIST Measurement Results*; NIST: 1994.

(43) Lashley, J. C.; et al. Critical examination of heat capacity measurements made on a Quantum Design physical property measurement system. *Cryogenics* **2003**, *43* (6), 369−378.

(44) Javorský, P.; Wastin, F.; Colineau, E.; Rebizant, J.; Boulet, P.; Stewart, G. Low-temperature heat capacity measurements on encapsulated transuranium samples. *J. Nucl. Mater.* **2005**, *344*, 50−55.

(45) *Final report of the TCOFF project (2020)*; www.oecd-nea.org/science/tcoff/, 2020.

(46) Zhou, M.; Jiang, X.; Li, C.; Lin, Z.; Yao, J.; Wu, Y. The double molybdate $Rb_2Ba(MoO_4)_2$: Synthesis, crystal structure, optical, thermal, vibrational properties, and electronic structure. *Z. Anorg. Allg. Chem.* **2015**, *641*, 2321−2325.

(47) Gudkova, I. A.; Solodovnikova, Z. A.; Solodovnikov, S. F.; Zolotova, E. S.; Kuratieva, N. V. Phase formation in $Li_2MoO_4-K_2MoO_4-MMoO_4$ (M= Ca, Pb, Ba) systems and the crystal structure of α-$KLiMoO_4$. *Russ. J. Inorg. Chem.* **2011**, *56*, 1443−1452.

(48) Chance, W. M.; Loye, H. C. Z. Synthesis, structure, and optical properties of a series of quaternary oxides, $K_2Ba(MoO_4)_2$ (M= Cr, Mo, W). *Solid State Sci.* **2014**, *28*, 90−94.

(49) Shannon, R. D. Revised Effective Ionic Radii and Systematic Studies of Interatomic Distances in Halides and Chaleogenides. *Acta Crystallogr., Sect. A: Cryst. Phys., Diffr., Theor. Gen. Crystallogr.* **1976**, *32*, 751−767.

(50) Schwarz, H. *Z. Anorg. Allg. Chem.* **1966**, *345*, 230−245.

(51) Grundmann, H.; Schilling, A.; Medarde, M.; Sheptyakov, D. V. Influence of disorder on the structural phase transition and magnetic interactions in $Ba_{3-x}Sr_xCr_2O_8$. *Phys. Rev. B* **2014**, *90*, 075101.

(52) Azdouz, M.; Manoun, B.; Essehli, R.; Azrour, M.; Bih, L.; Benmokhtar, S.; Hou, A. A.; Lazor, P. Crystal chemistry, Rietveld refinements and Raman spectroscopy studies of the new solid solution series: $Ba_{3-x}Sr_x(VO_4) − 2$ (0 < x < 3). *J. Alloys Compd.* **2010**, *498*, 42−51.

(53) Weller, M. T.; Skinner, S. J. $Ba_3Mn_2O_8$ determined from neutron powder diffraction. *Acta Crystallogr., Sect. C: Cryst. Struct. Commun.* **1999**, *55*, 154−156.

(54) Sahu, M.; Krishnan, K.; Nagar, B. K.; Jain, D.; Saxena, M. K.; Pillai, C. G. S.; Dash, S. Characterization and thermo physical property investigations on $Ba_{1-x}Sr_xMoO_4$ (x = 0, 0.18, 0.38, 0.60, 0.81, 1) solid-solutions. *J. Nucl. Mater.* **2012**, *427*, 323−332.

(55) Benigni, P.; Mikaelian, G.; Ruiz, E.; Perrin-Pellegrino, C.; Rogez, J. Calorimetric Determination of the Formation Enthalpies of Cs Polymolybdates at 298.15 K and 0.1 MPa. *J. Chem. Eng. Data* **2020**, *65* (8), 3875−3883.

(56) Gamsjäger, H.; Morishita, M. Thermodynamic properties of molybdate ion: reaction cycles and experiments. *Pure Appl. Chem.* **2015**, *87* (5), 461−478.

(57) O'Hare, P.A.G. Thermochemistry of molybdates III. Standard enthalpy of formation of barium molybdate, and the standard entropy and standard Gibbs energy of formation of the aqueous molybdate ion. *J. Chem. Thermodyn.* **1974**, *6* (5), 425−434.

(58) Shukla, N. K.; Prasad, R.; Sood, D. D. The standard molar enthalpies of formation at the temperature T = 298.15K of barium molybdate $BaMoO_4(cr)$ and strontium molybdate $SrMoO_4(cr)$. *J. Chem. Thermodyn.* **1993**, *25*, 429−434.

(59) Majzlan, J.; Navrotsky, A.; Woodfield, B. F.; Lang, B. E.; Boerio-Goates, J.; Fisher, R. A. Phonon, Spin-Wave, and Defect Contributions to the Low-Temperature Specific Heat of alpha-FeOOH. *J. Low Temp. Phys.* **2003**, *130* (1−2), 69−76.

(60) Woodfield, B. F.; Boerio-Goates, J.; Shapiro, J. L.; Putnam, R. L.; Navrotsky, A. Molar heat capacity and thermodynamic functions of zirconolite $CaZrTi_2O_7$. *J. Chem. Thermodyn.* **1999**, *31*, 245−253.

(61) Woodfield, B. F.; Shapiro, J. L.; Stevens, R.; Boerio-Goates, J.; Putnam, R. L.; Helean, K. B.; Navrotsky, A. Molar heat capacity and thermodynamic functions for $CaTiO_3$. *J. Chem. Thermodyn.* **1999**, *31*, 1573−1583.

(62) Smith, S. J.; Stevens, R.; Liu, S.; Li, G.; Navrotsky, A.; Boerio-Goates, J.; Wooodfield, B. F. Heat capacities and thermodynamic

functions of TiO_2 anatase and rutile: Analysis of phase stability. *Am. Mineral.* **2009**, *94*, 236−243.

(63) Gopal, E. S. *Specific heats at low temperatures*; Plenum Press: 1966.

(64) Rosen, P. F.; Woodfield, B. F. Standard methods for heat capacity measurements on Quantum Design Physical Property Measurement System. *J. Chem. Thermodyn.* **2020**, *141*, 105974.

(65) Shi, Q.; Zhang, L.; Schlesinger, M. E.; Boerio-Goates, J.; Woodfield, B. F. Low temperature heat capacity Study of $Fe(PO_3)_3$ and $Fe_2P_2O_7$. *J. Chem. Thermodyn.* **2013**, *61*, 51−57.

(66) Shi, Q.; Zhang, L.; Schlesinger, M. E.; Boerio-Goates, J.; Woodfield, B. F. Low temperature heat capacity study of $FePO_4$ and $Fe_3(P_2O_7)_2$. *J. Chem. Thermodyn.* **2013**, *62*, 35−42.

(67) Shi, Q.; Zhang, L.; Schlesinger, M. E.; Boerio-Goates, J.; Woodfield, B. F. Low temperature heat capacity study of Fe_3PO_7 and $Fe_4(P_2O_7)_3$. *J. Chem. Thermodyn.* **2013**, *62*, 86−91.

(68) Smith, A. L.; Kauric, G.; van Eijck, L.; Goubitz, K.; Wallez, G.; Griveau, J.-C.; Colineau, E.; Clavier, N.; Konings, R. J. M. Structural and thermodynamic study of dicesium molybdate $Cs_2Mo_2O_7$: Implications for fast neutron reactors. *J. Solid State Chem.* **2017**, *253*, 89−102.

(69) Smith, A. L.; Griveau, J.-C.; Colineau, E.; Raison, P. E.; Wallez, G.; Konings, R. J. M. Low temperature heat capacity of Na_4UO_5 and Na_4NpO_5. *J. Chem. Thermodyn.* **2015**, *91*, 245−255.

(70) Smith, A. L.; Colineau, E.; Griveau, J.-C.; Popa, K.; Kauric, G.; Martin, P.; Scheinost, A. C.; Cheetham, A. K.; Konings, R. J. M. A New Look at the Structural and Magnetic Properties of Potassium Neptunate K_2NpO_4 Combining XRD, XANES spectroscopy, and Low-Temperature Heat Capacity. *Inorg. Chem.* **2017**, *56*, 5839−5850.

(71) Morishita, M.; Fukushima, M.; Houshiyama, H. Third Law Entropy of Barium Molybdate. *Mater. Trans.* **2016**, *57*, 46−51.

(72) Osborne, D. W.; Flotow, H. E.; Hoekstra, H. R. Cesium molybdate, Cs_2MoO_4: Heat capacity and thermodynamic properties. *J. Chem. Thermodyn.* **1974**, *6*, 179−183.

(73) Guillaumont, R.; Fanghänel, T.; Fuger, J.; Grenthe, I.; Neck, V.; Palmer, D. A.; Rand, M. H. *Update on the chemical thermodynamics of uranium, neptunium, plutonium, americium and technetium; Update on the chemical thermodynamics of uranium, neptunium, plutonium, americium & technetium*; OECD Nuclear Energy Agency: Data Bank, 2003.

(74) Chase, M. W. *NIST-JANAF Thermochemical Tables*, 4th ed.; American Chemical Society, American Institute of Physics, National Bureau of Standards: New York, 1998; monograph 9.

(75) Cordfunke, E. H. P.; van der Laan, R. R.; van Miltenburg, J. C. Thermophysical and thermochemical properties of BaO and SrO from 5 to 1000 K. *J. Phys. Chem. Solids* **1994**, *55*, 77−84.

(76) Zolotova, E. S.; Solodovnikova, Z. A.; Yudin, V. N.; Solodovnikov, S. F.; Khaikina, E. G.; Basovich, O. M.; Korolkov, I. V.; Filatova, I. Y. Phase relations in the Na_2MoO_4-Cs_2MoO_4 and Na_2MoO_4-Cs_2MoO_4-$ZnMoO_4$ systems, crystal structures of $Cs_3Na(MoO4)_2$ and $Cs_3NaZn_2(MoO_4)_4$. *J. Solid State Chem.* **2016**, *233*, 23−29.

(77) The measured dissolution enthalpy was corrected to the molality of the certified enthalpy value $m = 0.111$ mol kg^{-1} using the relationship $\Delta H°(500H_2O, 298.15 K) = \Delta H(nH_2O, 298.15 K) − \{\Phi_L(nH_2O) − \Phi_L(500H_2O)\}$, where $\Delta H(nH_2O, 298.15 K)$ is the measured dissolution enthalpy corrected to the reference temperature and the term $\{\Phi_L(nH_2O) − \Phi_L(500H_2O)\}$, derived from Parker's tabulation in ref 33 and listed in ref 32, corrects the molality to the certified value. The uncertainty on the correction was estimated not to exceed 5 J mol^{-1}.[32]

(78) Average value of refs 36, 37, and 55,